Organosulfonate counteranionstrapped coordination polymer as highoutput triboelectric nanogenerator material for selfpowered anticorrosion

Document Version
Accepted author manuscript

CHEMISTRY
A European Journal

Accepted Article

Authors: Liwei Mi, Yingying Zhang, Jiarui Wu, Siwen Cui, Wutao Wei, Weihua Chen, Rui Pang, and Zijie Wu

COMMUNICATION

Organosulfonate counteranions-trapped coordination polymer as high-output triboelectric nanogenerator material for self-powered anticorrosion

Yingying Zhang,[a] Jiarui Wu,[a] Siwen Cui,[a] Wutao Wei,[a] Weihua Chen,[c] Rui Pang,*[b] Zijie Wu[d] and Liwei Mi*[a]

Dedication ((optional))

Abstract: Selection of the friction electrode materials is crucial to the performance of triboelectric nanogenerator (TENG). In the present study, a metal-organic coordination complex containing organosulfonate counteranions with electron-donating ability was synthesized via the coordination-driven self-assembly approach under mild reaction conditions and was chosen as positive electrode material to construct a triboelectric nanogenerator, having high-output performance with a peak value of short circuit current density of 98.6 µA and output voltage of 1180 V. As a practical application, it was shown to light up 1488 commercial green LEDs and power an anticorrosion system device to protect metals from corrosion.

The metal-organic coordination polymers (MOCPs), a subclass of crystalline materials comprised of inorganic metal nodes and organic linkers, have been deemed as potential candidates of ideal materials for many applications in various areas.[1-6] Among the application fields, considerable attention has been paid on the application of MOCPs in electricity, including the development of fuel cells,[7,8] supercapacitors,[9,10] thermoelectrics,[11,12] and others. Recently, the well-known metal-organic frameworks (MOFs), also known as porous coordination polymers, have been used as triboelectric nanogenerator (TENG) materials for self-powered systems and sensor applications,[13,14] which is advantageous not only for extending the advanced materials of TENG but also for expanding the application range of MOCPs. However, the development of MOCPs-based TENG with high-output performance for various applications is still challenging.

As a new type of energy storage and output device that can convert all kinds of mechanical energy into electrical energy, TENG is regarded as a sustainable and renewable energy source and has been widely applied in self-powered sensors,[15-17] wearable devices,[18-20] self-powered electrochemical cathodic protection,[21-25] batteries and supercapacitors[26-29] since they were first present in 2012.[30] In general, the output of TENG is highly dependent on the structure design of TENG device, the frictional motions, the environmental factors, especially on the nature of the friction pair materials. For MOCP-based TENG, it is particularly important to design and assemble compounds with specific structures. In the assembly process, it is crucial to filter multifunctional organic linkers to construct a diversity of coordination polymers. In contrast to the studies on the most common organocarboxylate linkers,[31-33] the coordination chemistry of organosulfonate ligands has been given less attention,[34-39] probably due to their weak coordinating ability. Organosulfonates are ligated with the transition metals so weakly that they are still as free counteranions,[40,41] forming the one-/two-dimensional (1D/2D) polymer structure but presenting higher dimensional architectures via hydrogen bonds and π-π interactions in the existence of other aromatic organic ligands. These architectures with highly conjugated structures might be ideal candidates for various applications. Herein we report the straightforward synthesis and structural characterization of an expanded 3D supramolecular MOCP [{Co(bipy)(H₂O)₄}·(3-OH-2,7-NDS)·2H₂O]ₙ (**1**) constructed from 3-hydroxy-2,7-naphthalenedisulfonate (3-OH-2,7-NDS) and 4,4'-bipyridine (bipy) with transition metal Co(II). A novel TENG based on complex **1** was designed, which was introduced into the cathodic protection system for protecting metals from corrosion.

Complex **1** was prepared by the dropwise addition of bipy in methanol into the mixture solution of 3-hydroxy-2,7-naphthalenedisulfonate (3-OH-2,7-NDS) and Co(NO₃)₂·6H₂O in distilled water at room temperature. Single-crystal X-ray diffraction reveals that complex **1** contained 1D coordination electriferous linear chains of [Co(bipy)(H₂O)₄]²⁺ and free 3-OH-2,7-NDS as counterions (Figure. 1b). The center metal ion Co(II) is in representative hexacoordinated octahedral coordination geometry formed by four oxygen atoms from water molecules and two nitrogen atoms from bipy bridges. The [Co(bipy)(H₂O)₄]²⁺ chains interconnect along the plane, counterions 3-OH-2,7-NDS are embedded between the 1D chains by π-π interactions, resulting in the 2D sandwich structure (Figure. 1b). Stacking of 2D sandwich through H-bonding interactions between coordinated waters, free water molecules and 3-OH-2,7-NDS yield three-dimensional (3D) supramolecular structure (Figure. 1c). The

[a]   Y. Zhang,[+] J. Wu,[+] S. Cui,[+] W. Wei, L. Mi
       Center for Advanced Materials Research
       Zhongyuan University of Technology
       Zhengzhou 450007, P. R. China
       E-mail: mlwzzu@163.com
[b]   R. Pang
       International Laboratory for Quantum Functional Materials of Henan
       and School of Physics and Engineering
       Zhengzhou University
       Zhengzhou 450001, P. R. China
       E-mail: pangrui@zzu.edu.cn
[c]   W. Chen
       College of Chemistry and Molecular Engineering
       Zhengzhou University
       Henan 450001, P. R. China
[d]   Z. Wu
       North West Composites Centre, School of Materials
       University of Manchester, Manchester M13 9PL, UK
[+]These authors contributed equally to this work.

       Supporting information for this article is given via a link at the end of the document.((Please delete this text if not appropriate))
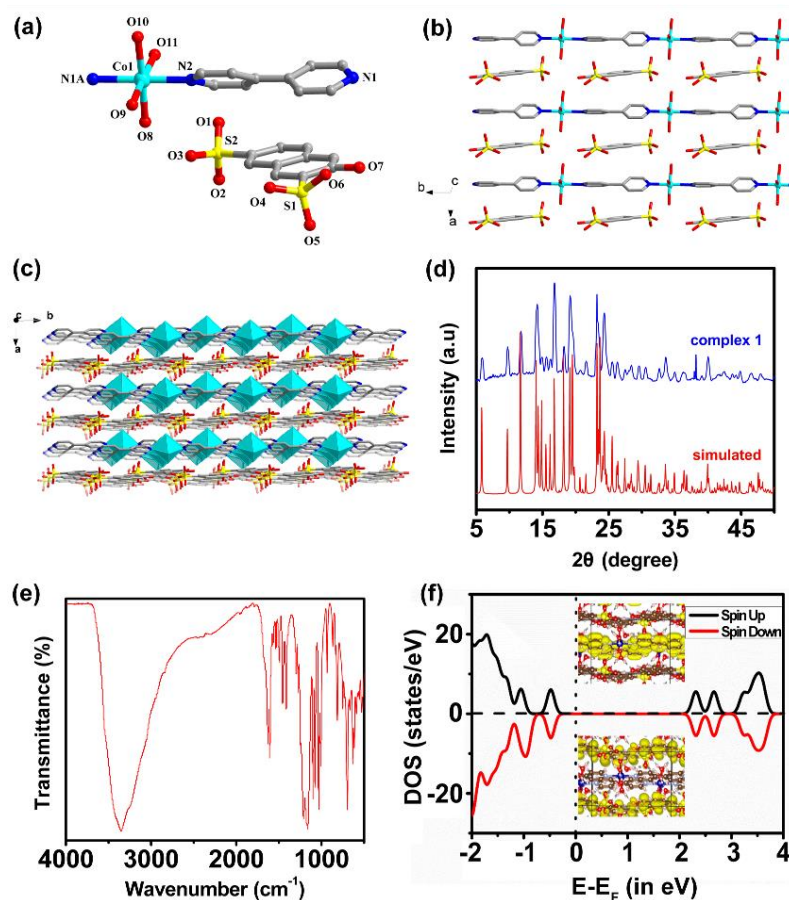
COMMUNICATION

Figure 1. (a) The asymmetric unit of crystal structure for **1**.[42] (b) 2D sandwich structure and (c) 3D supramolecular network of **1**. Solvent molecules and hydrogen atoms were omitted for clarity. (d) PXRD and the corresponding simulated patterns for **1**. (e) FT-IR. (f) The state density distribution and the frontier molecular orbitals of **1** (inside) using the plane-wave-basis-set Vienna ab initio simulation package (VASP).

powder X-ray diffraction (PXRD) pattern of **1** is in good agreement with the simulated (Figure. 1d). The Fourier transform infrared spectroscopy (FT-IR) (Figure. 1e) confirmed the existence of the sulfonate and O-H groups with peaks at 1033-1211 cm^{-1} and a broad absorption at 3354 cm^{-1}, respectively.

UV-Visible diffuse reflectance spectroscopy (UV−Vis DRS) was employed to estimate the bandgap of powder samples (Figure. S1)[43]. The bandgap energy (E_g) of complex **1** is approximately 3.42 eV by a Tauc plot (Figure. S2). Meanwhile, the Mott–Schottky measurements were explored to elucidate the semiconductor nature of **1**. The slope of the obtained C^{-2} versus the potential plot is positive, indicating that complex **1** can be considered as an n-type semiconductor (Figure. S3). The material can be also confirmed to be a semiconductor via the density-functional theory (DFT) calculations. Furthermore, the entire structure of **1** is highly conjugated (Figure. 1f), in which the delocalization of the π-electron cloud might make the electron transfer easier.

Generally, the nature of the friction pair materials (including the polarity, shape and size) plays an important role in the output performance of TENG.[44,45] Materials with micro/nanostructures have larger specific surface area that could enhance the charge density in the friction process, so the flake sample **1** was milled

into powder to expand the specific surface area and coated on copper tape (Figure. 3a). After grinding, the morphology of complex **1** changed from light-pink bulk crystals to powders with much smaller particle size (Figure. 2), which is helpful in enhancing the output performance of TENG.

In addition, Nylon-6 (NY), polyvinylidene fluoride (PVDF) and powder **1** electrodes were matched in pairs for current signal measurements to determine the polarity of complex **1**. Compared with the direction of the output signals for NY/PVDF, two well-known triboelectric friction materials with positive and negative triboelectric polarities, respectively, the triboelectric polarity of the MOCP powder can be ascertained. As shown in Figure. S4, the maximum output value is PVDF/NY group, while that of the MOCP powder/NY is the minimum, suggesting that the MOCP powder has the similar positive triboelectric polarity as NY, and NY has greater positive triboelectric polarity than MOCP powder. Thus, the triboelectric polarity order from positive to negative is Nylon, complex **1**, PVDF. Besides, to further improve the output performance of TENG, PVDF solution was spin-coated on Kapton film, which has good ability to store the triboelectrification charges,[46] generating more induced charges and higher external current (Figure. 3a).

COMMUNICATION

The working principle of TENG based on MOCP powder and PVDF electrodes in the traditional vertical contact-separation mode is shown in Figure. 3b. It is acknowledged that coupling effect of contact initiation and electrostatic induction generates the electricity from TENG.[47,48] No current signal is detected in the external circuit without external mechanical stimulation (Figure. 3b(i)). When an external force was applied to make the two active triboelectric layers contact with each other, electrons of powder **1** were injected into PVDF, leading to the accumulation of negative charge on the surface of PVDF while MOCP powder was positively charged (Figure. 3b(ii)). When the two electrodes were separated, the back electrode (Cu layer) was positively charged due to the electrostatic induction, which is contrary to the charge of PVDF, and the potential difference between these two electrodes caused the current flow from the MOCP powder electrode to the PVDF electrode (Figure. 3b(iii)). No current is generated in the external circuit as charge balance is achieved (Figure. 3b(iv)). Later, the potential difference diminishes due to the reduced distance between these two electrodes when the external force is applied again, causing the converse flow of current from the PVDF electrode to the MOCP powder (Figure. 3b(v)) until the charge accumulation reaches a new equilibrium

(Figure. 3b(ii)). Figure. 3c shows the generation of a periodic short current in the contact-separation process.

The output performance of **1**-based TENG controlled via a linear motor moving back and forth at 5 Hz with a contact area of 5 cm x 5 cm is illustrated in Figure. 4a-d. In the case of short circuit, momentary current is produced to counterpoise the
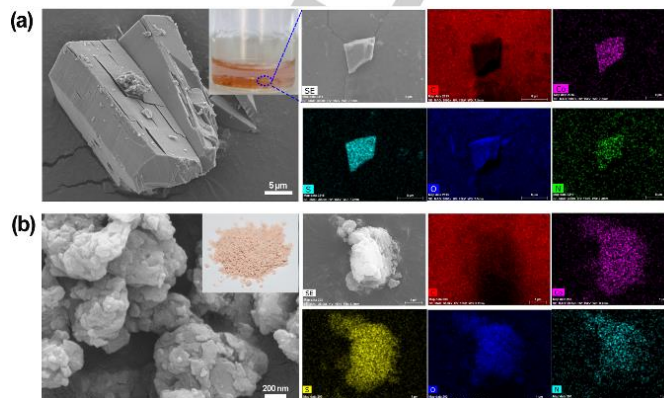

Figure 2. FE-SEM images, EDS mapping analysis and digital photos (inset) of complex **1** (a) before and (b) after grinding.
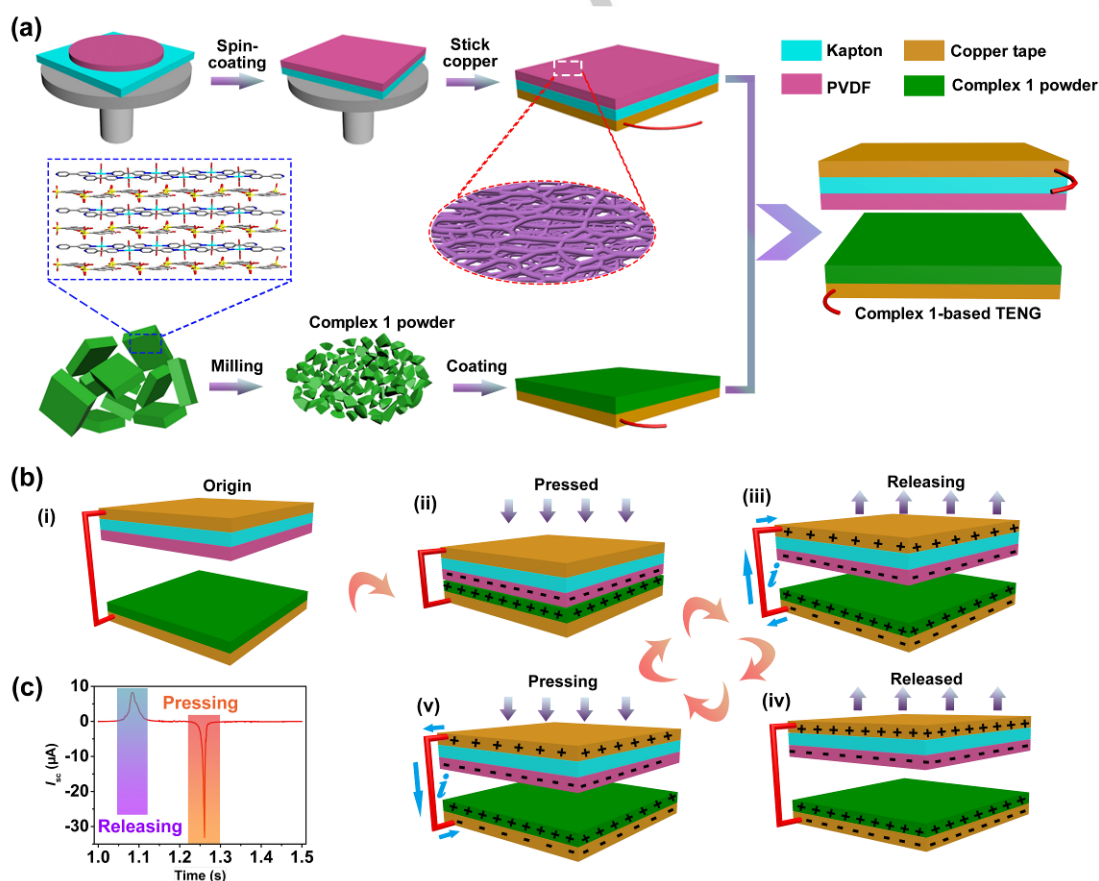

Figure 3. (a) The schematic diagram of the fabrication process of 1-based TENG. (b) Working principle of 1-based TENG. (c) A periodic current in the contact-separation process.
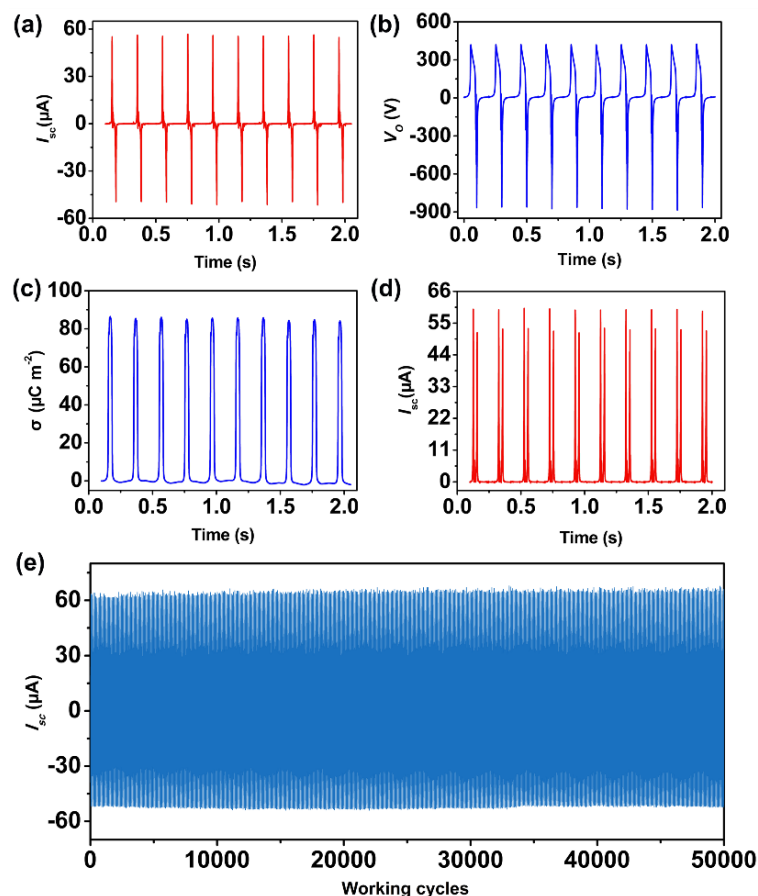
COMMUNICATION

Figure 4. (a) I_{sc}, (b) V_o, (c) σ of **1**-based TENG and (d) I_{sc} with a rectifier bridge to make it in the same direction. (e) I_{sc} of **1**-based TENG after working 50000 cycles.
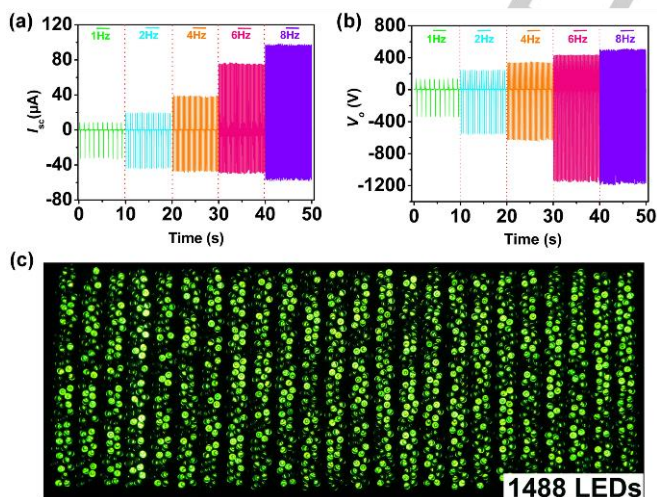

Figure 5. (a) I_{sc} and (b) V_o from 1 Hz to 8 Hz. (c) Photograph of lighting 1488 LEDs powered by **1**-based TENG at 8 Hz.

electric potential difference caused by friction. As indicated in Figure. 4a and 4b, the peak value of short circuit current (I_{sc}) and

output voltage (V_o) on the verge of 58.3 µA and 890 V, respectively. Charge density (σ), as a criterion for evaluating material availability,[21,49,50] is approximately 86 µC m^{-2} (Figure. 4c), which is close to that of the TENGs based on the most widely used triboelectric materials, including various polymers and metals.[16,46] From the durability tests at 5 Hz (Figure. 4e and Figure S5), it can be seen that both the I_{sc} and V_o output of electrode material holds stable and no downward trend is observed after working for 50,000 cycles. Meanwhile, the surface morphology of the friction layers remained basically after operation (Figure S6). Both above indicate that the materials have an outstanding stability and friction resistance.

In addition to the relative polarity between the two friction electrodes materials, the frequency of TENG operation also plays a crucial role in improving the output performance.[51] Therefore, the I_{sc} and V_o from 1 Hz to 8 Hz operating frequencies were measured (Figure. 5a and 5b). I_{sc} and V_o reaches the maximum value of 98.6 µA and 1180 V at 8 Hz, respectively, which could light up 1488 commercial green LEDs.

Figure. S7 shows the I_{sc} under various loading resistance to calculate the maximum output power. I_{sc} decreases with the increase in the connected external resistances and the corresponding peak power appears at approximately 26.4 mW with an equivalent load resistance of 40 MΩ. Meanwhile, the
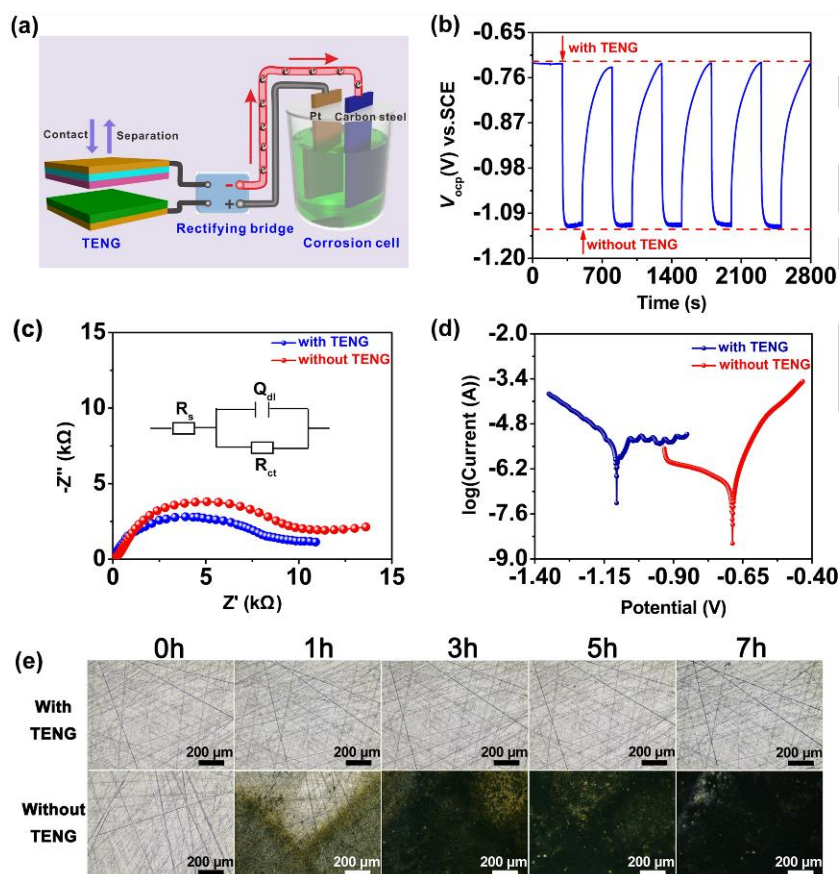
COMMUNICATION

Figure 6. (a) Schematic diagram of the cathodic protection of Q235 carbon steel by the **1**-based TENG. (b) OCP cycle, (c) EIS and equivalent circuit (inset), and (d) Tafel curves of the carbon steel connected with TENG and without TENG, respectively. (e) Microscopic photographs of the carbon steel immersed in 3.5 wt% NaCl solution for 1 h, 3 h, 5 h and 7 h coupled with and without TENG, respectively.

Table 1. Resistance parameters obtained from fitting process of Q235 carbon steel with and without **1**-based TENG connection

	R_s (Ω)	Q		R_{ct} (Ω)
		Y(s·sec^n)	n	
With TENG	78.48	2.387×10^{-5}	0.8064	9106
Without TENG	70.28	7.782×10^{-5}	0.6531	13930

symmetrical supercapacitors using active carbon as electrode (potential window from 0 to 0.9 V) were assembled and charged by the output of **1**-based TENG to evaluate its suitability for practical applications. The voltage of the supercapacitor device increases rapidly at the beginning of charging but gradually as time goes on (Figure S8a) because of its self-discharge behavior, and the supercapacitor charged at 0.473 V can discharge for 788 s (Figure. S8b). The calculated capacitance of the device was 8.3 mF at a galvanostatic current of 5 µA.

In consideration of excellent output performance of **1**-based TENG, it was applied for impressing current cathodic protection of carbon steel. As shown in Figure. 6a, **1**-based TENG is connected with a rectifier bridge, and the protected Q235 carbon

steel is linked with the negative electrode of TENG while the platinum electrode is connected to the positive. When the TENG goes into operation, the generated electrons are injected into the surface of the protected metal, resulting in a cathodic polarization to limit further electrochemical reaction.

To evaluate the cathodic protection efficiency, the open circuit potential (OCP) of the protected metal, the electrochemical impedance spectroscopy (EIS) and the electrochemical polarization curves of the corrosion system with and without the TENG were tested using a three-electrode system. The OCP of the protected metal stabilizes at -0.72 V (*vs.* SCE) without the TENG while the value of the OCP rapidly declines to -1.11 V (*vs.* SCE) once the carbon steel is coupled with the TENG. This negative shift can be attributed to the increasing number of transferred charges, showing effective cathodic protection by the TENG. After removing **1**-based TENG, the OCP value returns to its original value (Figure. 6b). As shown in Figure. 6c, the radius of semi-circle of transfer charge resistance (R_{ct}) produced with TENG is smaller than that connecting without TENG, which proves the effectiveness of external current cathodic protection again. For directly explaining the impedance spectra, the equivalent circuit diagram was selected according to the fitting process (inset of Figure. 6c). Parameters of equivalent circuit including R_s (the solution resistance), R_{ct} and Q_{dl} (the double-layer

COMMUNICATION

capacitor parallel to R_{ct}) analyzed from the Nyquist plots are listed in Table 1. In addition, corrosion potential (E_{corr}) with TENG is much lower than that without TENG connection due to the increasing transfer electrons (Figure. 6d and Table 2), which are corresponding well to the OCP change. On the contrary, corrosion current (I_{corr}) coupled with TENG is slightly higher than that without TENG because the electrochemical reaction is strengthened by the increasing number of electrons on the Q235 carbon steel surface generated by TENG. These results also prove the feasibility of the cathodic protection for Q235 carbon steel when MOCP-based TENG serves as the power supplier.

To further characterize the effect of TENG cathodic protection directly, immersion experiments for 1 h, 3 h, 5 h and 7 h with and without **1**-based TENG were conducted, respectively. The microscopy images (Figure. 6e) show the absence of obvious rusts on the carbon steel attached to TENG even after 7 h, while on the carbon steel without TENG, rust appears after 1 h. The number of rust stains increase with the increase of immersion time, implying that the generated electrons from **1**-based TENG effectively suppress cathodic protection. Furthermore, the corrosion products on the surface of carbon steel were analyzed by EDS spectra (Figure S9). Obviously, the oxygen content of the corrosion products on the carbon steels coupled with TENG is much lower than the corresponding content without TENG protection, indicating that there was much less rust formed oncarbon steels when they were cathodic protected by TENG, which also proves the effectively cathodic protection.

Table 2. Electrochemical parameters received from polarization curves of Q235 carbon steel with and without MOCP-based TENG connection

	E_{corr} (V(vs.SCE))	I_{corr} (µA)	-β_c (mv dec^{-1})	β_a (mv dec^{-1})
With TENG	-1.126	15.28	6.120	0.624
Without TENG	-0.7138	0.217	2.442	16.709

In summary, a coordination polymer containing organosulfonate counterions was synthesized and was utilized as an active electrode material for TENGs. The as-designed **1**-based TENG provides a sustainable high-output performance of approximately 98.6 µA and 1180 V and shows a good stability even after 50000 cycles. Moreover, it can serve as a power supplier to protect Q235 carbon steel from corrosion. Our results not only further enrich the application areas of MOCPs, but also provide a theoretical foundation and experimental evidence for the design and construction of TENGs with high-output performance.

Experimental Section

Materials

All reagents and solvents in this work were obtained commercially and used without any further purification.

Preparation of complex 1

4,4'-bipyridine (78 mg, 0.05 mmol) in 2 mL methanol was added dropwise to the mixture of disodium 3-Hydroxy-2,7-naphthalenedisulfonate (174 mg, 0.05 mmol) in 1 mL distilled water and $Co(NO_3)_2 \cdot 6H_2O$ (291 mg, 0.1 mmol) in 4 mL methanol. The final mixture was stirred for 10 min and then filtered. Light pink crystals were obtained after one week. Yield: 70%. Elemental analysis calcd (%) for $C_{20}H_{26}N_2O_{13}S_2Co$: C 38.40, H 4.19, N 4.48, found C 38.79, H 4.01, N 4.76. IR (KBr, cm^{-1}): 3354 (s), 1629 (m), 1609 (m), 1541 (w), 1497 (w), 1455 (m), 1415 (m), 1295 (w), 1270 (w), 1211 (m), 1158 (s), 1100 (m), 1073 (m), 1033 (m), 814 (m), 695 (m), 634(m), 615(m), 590(w), 529(w), 480(w).

Computational section

Calculations were performed using the plane-wave-basis-set Vienna ab initio simulation package (VASP).[52] A 4×4×4 K-point sampling was used to sample the Brillouin zone. Projector augmented wave potentials were employed with a kinetic energy cutoff of 425 eV.[53] For the exchange-correlation functional, the Perdew-Burke-Ernzerh of generalized gradient approximation was utilized[54] and DFT-D2 method was used to evaluate the van der Waals interactions between the organics.[55] A Hubbard U = 7 eV and J = 1 eV was used to evaluate correlation effects of 3d electrons on Co. The Gaussian smearing with 0.1 eV was used to smooth the occupancy in all calculations. The structural relaxation was end till the forces on each atom is less than 0.01 eV/Å.

Fabrication of 1-based TENG

The fabrication process of **1**-based TENG is shown in Figure. 2a. The negative triboelectric electrode with PVDF was prepared according to the literature.[22,24] Unlike the preparation process of PVDF electrode, MOCP samples **1** were preground mechanically, and then paved uniformly and fixed firmly on the sticky side of the Cu tape. An air gun was used to remove the redundant powder. Finally, a Cu wire was attached on the other side of the Cu tape by conductive silver epoxy. Combine the positive part with MOCP materials and the negative part with PVDF together, the **1**-based TENG was obtained. The vertical contact-separation mode of TENG was used, and the effective contact area is 5×5 cm^2.

Characterization

The FI-IR spectra were accomplished on Thermo iS50 FT-IR with KBr pellets in the 400-4000 cm^{-1}. UV–Vis absorption spectra were recorded on a Shimadzu UV-2600 spectrophotometer with a white standard of $BaSO_4$ as a reference. Powder X-ray diffraction (PXRD) patterns were carried out on Bruker D8 Advance X-ray powder diffractometer with Cu-Kα irradiation at a scan rate of 0.1ºs^{-1}. The morphologies and sizes of the samples were observed by using Zeiss Merlin Compact field emission scanning electron microscope (FE-SEM) equipped with an energy-dispersive X-ray spectroscopy (EDS) system. The short circuit current (I_{sc}) and the output voltage (V_o) were tested by a SR570 low-noise current amplifier (Stanford Research System) and a NI-PCI6259 (National Instruments) with a load resistor of 100 MΩ, respectively. The electrochemical measurements including open circuit potential (OCP) changes and Tafel curves of carbon steel coupled with and without the MOCP-based TENG were tested in a three-electrode system using an electrochemical workstation (CHI 660E, Shanghai Chenhua Instrument Co., Ltd, China) in the 3.5 wt.% NaCl solution and the discharge time of the active carbon supercapacitor was recorded on a galvanostatic charge/discharge tester (CT2001A). The carbon steel, a platinum foil, and a saturated calomel electrode (SCE) were used as the working electrode, counter electrode, and reference electrode, respectively. Tafel curves were measured at a scan rate of 1 mV/s. The protecting effect of Q235 carbon steel was observed by using 4X metallographic microscope.

COMMUNICATION

[1]. L. Zhu, X.-Q. Liu, H.-L. Jiang, L.-B. Sun, *Chem. Rev.*, **2017**, *117*, 8129-8176.

[2]. W. P. Lustig, S. Mukherjee, N. D. Rudd, A. V. Desai, J. Li, S. K. Ghosh, *Chem. Soc. Rev.*, **2017**, *46*, 3242-3285.

[3]. B. Van de Voorde, B. Bueken, J. Denayer, D. De Vos, *Chem. Soc. Rev.*, **2014**, *43*, 5766-5788.

[4]. P. Horcajada, R. Gref, T. Baati, P. K. Allan, G. Maurin, P. Couvreur, G. Ferey, R. E. Morris, C. Serre, *Chem. Rev.*, **2012**, *112*, 1232-1268.

[5]. L. Zhang, H. Liu, W. Shi, P. Cheng, Coord. *Chem. Rev.*, **2019**, *388*, 293-309.

[6]. Y.-Y. Zhang, W.-X. Gao, L. Lin, G.-X. Jin, *Coord. Chem. Rev.*, **2017**, *344*, 323-344.

[7]. M. Inukai, S. Horike, T. Itakura, R. Shinozaki, N. Ogiwara, D. Umeyama, S. Nagarkar, Y. Nishiyama, M. Malon, A. Hayashi, T. Ohhara, R. Kiyanagi, S. Kitagawa, J. Am. Chem. Soc., **2016**, *138*, 8505-8511.

[8]. M. Yoon, K. Suh, S. Natarajan, K. Kim, *Angew. Chem. Int. Ed.*, **2013**, *52*, 2688-2700.

[9]. X. Cao, C. Tan, M. Sindoro, H. Zhang, *Chem. Soc. Rev.*, **2017**, *46*, 2660-2677.

[10]. R. R. Salunkhe, Y. V. Kaneti, J. Kim, J. H. Kim, Y. Yamauchi, *Acc. Chem. Res.*, **2016**, *49*, 2796-2806.

[11]. B. Kim, J. Na, H. Lim, Y. Kim, J. Kim, E. Kim, *Adv. Funct. Mater.*, **2019**, *29*, 1807549.

[12]. L. Sun, B. Liao, D. Sheberla, D. Kraemer, J. Zhou, E. A. Stach, D. Zakharov, V. Stavila, A. A. Talin, Y. Ge, M. D. Allendorf, G. Chen, F. Leonard, M. A. Dinca, *Joule*, **2017**, *1*, 168-177.

[13]. G. Khandelwal, A. Chandrasekhar, N. P. Maria Joseph Raj, S. J. Kim, *Adv. Energy Mater.*, **2019**, *9*, 1803581.

[14]. R. Wen, J. Guo, A. Yu, J. Zhai, Z. L. Wang, *Adv. Funct. Mater.*, **2019**, *29*, 1807655.

[15]. M. Ma, Q. Liao, G. Zhang, Z. Zhang, Q. Liang, Y. Zhang, *Adv. Funct. Mater.*, **2015**, *25*, 6489-6494.

[16]. S. Cui, Y. Zheng, T. Zhang, D. Wang, F. Zhou, W. Liu, *Nano Energy*, **2018**, *49*, 31-39.

[17]. G. Khandelwal, A. Chandrasekhar, R. Pandey, N. P. Maria Joseph Raj, S.-J. Kim, *Sens. Actuators B: Chem.*, **2019**, *282*, 590-598.

[18]. J.-H. Zhang, J. Li, J. Du, X. Hao, H. Huang, *J. Mater. Chem. A*, **2019**, *7*, 11724-11733.

[19]. A. R. Mule, B. Dudem, S. A. Graham, J. S. Yu, *Adv. Funct. Mater.*, **2019**, *29*, 1807779.

[20]. Z. Liu, H. Li, B. Shi, Y. Fan, Z. L. Wang, Z. Li, *Adv. Funct. Mater.*, **2019**, *29*, 1808820.

[21]. S. Cui, Y. Zheng, J. Liang, D. Wang, *Chem. Sci.*, **2016**, *7*, 6477-6483.

[22]. S. Cui, Y. Zheng, J. Liang, D. Wang, *Nano Res.*, **2018**, *11*, 1873-1882.

[23]. W. Guo, X. Li, M. Chen, L. Xu, L. Dong, X. Cao, W. Tang, J. Zhu, C. Lin, C. Pan, Z. L. Wang, *Adv. Funct. Mater.*, **2014**, *24*, 6691-6699.

[24]. Z. Wang, L. Cheng, Y. Zheng, Y. Qin, Z. L. Wang, *Nano Energy*, **2014**, *10*, 37-43.

[25]. H. Zhang, S. Zhang, G. Yao, Z. Huang, Y. Xie, Y. Su, W. Yang, C. Zheng, Y. Lin, *ACS Appl. Mater. Inter.*, **2015**, *7*, 28142-28147.

[26]. T. Gao, K. Zhao, X. Liu, Y. Yang, *Nano Energy*, **2017**, *41*, 210-216.

[27]. Z. Wang, Z. Ruan, W. S. Ng, H. Li, Z. Tang, Z. Liu, Y. Wang, H. Hu, C. Zhi, *Small Methods*, **2018**, *2*, 1800150.

[28]. A. Maitra, S. Paria, K. S. Karan, R. Bera, A. Bera, A. K. Das, S. K. Si, L. Halder, A. De, B. B. Khatua, *ACS Appl. Mater. Inter.*, **2019**, *11*, 5022-5036.

[29]. X. Liu, K. Zhao, Z. L. Wang, Y. Yang, *Adv. Energy Mater.*, **2017**, *7*, 1701629.

[30]. F.-R. Fan, Z.-Q. Tian, Z. L. Wang, *Nano Energy*, **2012**, *1*, 328-334.

[31]. H. Furukawa, K. E. Cordova, M. O'Keeffe, O. M. Yaghi, *Science*, **2013**, *341*, 1230444.

[32]. W. Lu, Z. Wei, Z.-Y. Gu, T.-F. Liu, J. Park, J. Park, J. Tian, M. Zhang, Q. Zhang, T. Gentle, M. Bosch, H.-C. Zhou, *Chem. Soc. Rev.*, **2014**, *43*, 5561-5593.

[33]. M. Eddaoudi, H. L. Li, O. M. Yaghi, *J. Am. Chem. Soc.*, **2000**, *122*, 1391-1397.

[34]. A. P. Côté, G. K. H. Shimizu, *Coord. Chem. Rev.*, **2003**, *245*, 49-64.

[35]. A. V. Desai, B. Joarder, A. Roy, P. Samanta, R. Babarao, S. K. Ghosh, *ACS Appl. Mater. Inter.*, **2018**, *10*, 39049-39055.

[36]. G. K. H. Shimizu, R. Vaidhyanathan, J. M. Taylor, *Chem. Soc. Rev.*, **2009**, *38*, 1430-1449.

[37]. C. Zitzer, T. W. T. Muesmann, J. Christoffers, C. Schwickert, R. Pöttgen, M. S. Wickleder, *CrystEngComm*, **2014**, *16*, 11064-11077.

[38]. P. K. Allan, B. Xiao, S. J. Teat, J. W. Knight, R. E. Morris, *J. Am. Chem. Soc.*, **2010**, *132*, 3605-3611.

[39]. G. Zhang, H. Yang, H. Fei, *ACS Catal.*, **2018**, *8*, 2519-2525.

[40]. F. Gándara, C. Fortes-Revilla, N. Snejko, E. Gutiérrez-Puebla, M. Iglesias, M. A. Monge, *Inorg. Chem.*, **2006**, *45*, 9680-9687.

[41]. P. Kanoo, K. L. Gurunatha, T. K. Maji, *Cryst. Growth Des.*, **2009**, *9*, 4147-4156.

[42]. Crystal data, data collection parameters, and the results of the analysis of complex **1** are listed in Table S1. CCDC 1944746 (**1**) contain the supplementary crystallographic data for this paper. These data can be obtained free of charge from The Cambridge Crystallographic Data Centre via www.ccdc.cam.ac.uk/data_request/cif.

[43]. H. Q. Xu, J. Hu, D. Wang, Z. Li, Q. Zhang, Y. Luo, S. H. Yu, H. L. Jiang, *J. Am. Chem. Soc.*, **2015**, *137*, 13440-13443.

[44]. F. R. Fan, W. Tang, Z. L. Wang, *Adv. Mater.*, **2016**, *28*, 4283-4305.

[45]. X. S. Zhang, M. D. Han, R. X. Wang, F. Y. Zhu, Z. H. Li, W. Wang, H. X. Zhang, *Nano Lett.*, **2013**, *13*, 1168-1172.

[46]. Y. Yang, Y. Zheng, G. Zhang, D. Wang, F. Zhou, W. Liu, *Nano Energy*, **2017**, *38*, 467-476.

[47]. G. Zhu, C. Pan, W. Guo, C. Y. Chen, Y. Zhou, R. Yu, Z. L. Wang, *Nano Lett.*, **2012**, *12*, 4960-4965.

[48]. Z. L. Wang, *ACS nano*, **2013**, *7*, 9533-9557.

[49]. Z. L. Wang, *Faraday Discuss.*, **2014**, *176*, 447-458.

[50]. Y. Zi, S. Niu, J. Wang, Z. Wen, W. Tang, Z. L. Wang, *Nat. Commun.*, **2015**, *6*, 8376.

[51]. M.-L. Seol, S.-H. Lee, J.-W. Han, D. Kim, G.-H. Cho, Y.-K. Choi, *Nano Energy*, **2015**, *17*, 63-71.

[52]. G. Kresse, J. Furthmüller, *Comp. Mater. Sci.*, **1996**, *6*, 15-50.

[53]. G. Kresse, D. Joubert, *Phys. Rev. B*, **1999**, *59*, 1758-1775.

[54]. J. P. Perdew, K. Burke, M. Ernzerhof, *Phys. Rev. Lett.*, **1996**, *77*, 3865-3868.

[55]. S. Grimme, *J. Comput. Chem.*, **2006**, *27*, 1787-1799.

WILEY-VCH

COMMUNICATION

Entry for the Table of Contents (Please choose one layout)

Layout 1:

COMMUNICATION

An organosulfonate-contained cobalt(II) coordination complex was synthesized and taken as positive friction material to construct triboelectric nanogenerator (TENG) for self-powered electrochemical cathodic protection.
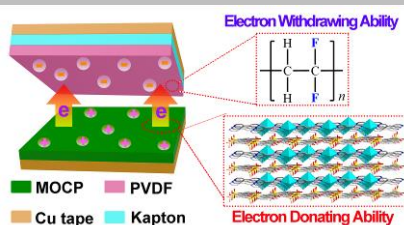
Yingying Zhang,[a] Jiarui Wu,[a] Siwen Cui,[a] Wutao Wei,[a]Weihua Chen,[c] Rui Pang,[b] Zijie Wu,[d] and Liwei Mi*[a]*

Page No. – Page No.

Organosulfonate counteranions-trapped coordination polymer as high-output triboelectric nanogenerator materials for self-powered anticorrosion